Measurement and Modeling of the Nanofiber Surface Potential during Electrospinning on a Patterned Collector: Toward Directed 3D Microstructuration

Meng Liang, Anne Hébraud, Christophe Sutter, Antoine Bardin, Emeline Lobry, Guy Schlatter

Measurement and modeling of the nanofiber surface potential during electrospinning on a patterned collector: towards directed 3D micro-structuration

*Dr. Meng Liang, Dr. Anne Hébraud, Christophe Sutter, Dr. Antoine Bardin, Dr. Emeline Lobry and Prof. Guy Schlatter**

ICPEES, Institut de Chimie et Procédé pour l'Energie, l'Environnement et la Santé, CNRS UMR 7515, Université de Strasbourg, 25 rue Becquerel, 67087 Strasbourg Cedex 2, France.

E-mail: Guy Schlatter, guy.schlatter@unistra.fr

Keywords: electrospinning; microfabrication; microstructured mats; modeling;

Abstract

Electrospinning allows the fabrication of microstructured mats when the nanofiber is deposited on a patterned collector made of regularly distributed protuberances. Such directed self-assembling strategy results from the building of an electrostatic template induced by the charged deposited fiber strands suspended between the protuberances which in turns induces a field of attractive and repulsive forces that guide the deposition of the fiber during its landing. However, after a certain time of electrospinning the microstructuration of the mat is generally subjected to modification and is eventually lost. Here, it is shown that the measurement of the surface potential above the deposited nanofibers is a powerful tool to track the evolution of the fibrous microstructuration during the fabrication. First, the electrospinning above a single and adjustable gap is deeply investigated and a model is proposed to explain the surface potential kinetics as a function of the gap size and the processed polymer solution. Then, the surface potential kinetics is correlated with the evolution of the 3D microstructuration in the case of electrospinning on a micropatterned collector. This original strategy paves the way for the controlled fabrication of 3D microstructured mats dedicated to a wide range of applications.

1. Introduction

Electrospinning,[1,2] as other techniques such as centrifugal spinning,[3] forcespinning,[4] or blowspinning,[5,6] allows the production of 3D nanofibrous membranes for a large number of applications ranging from energy, environment and health. Advantages and disadvantages of these spinning methods have been recently presented and discussed.[7] The conventional setups of all these spinning methods result in 3D non-structured mats consisting of randomly deposited nanofibers. Some of these spinning methods, such as electrospinning or solution blowspinning, can moreover produce nanofiber yarns and mats with aligned fibers when the deposition is carried out on a high-speed rotating drum.[8] However, one of the advantages of electrospinning over its competitors is its ability to guide the deposition of the nanofiber on micropatterned collectors by appropriately exploiting the Coulomb's electrostatic forces allowing thus the building of mats with a wider diversity of fibrous structures.[9–11] In this context, 1D aligned,[12] 2D[9] and even 3D[13,14] microstructured nanofibrous mats can be obtained paving the way for various practical applications such as the elaboration of biomimetic scaffolds mimicking bone osteons,[15–17] increasing the alignment and porosity of the mats for better cell colonization in tissue engineering,[18] improving the efficiency and reepithelialization of wound healing,[19] inducing anisotropic mechanical properties enhancing the biomimicry[20] and even improving the light transmittance and pollutant filtration of membranes.[21–23] It has been shown that the

charges carried by the suspended fibers hanging between the protuberances of patterned collectors play the most important role as they build an electrostatic template necessary for the controlled deposition of the electrospun fibers.[14,24] Experiments and numerical simulations demonstrated that this electrostatic template induces (i) a repulsive force above the suspended fibers and (ii) an attractive force above the fibers stacked on the collector protuberances. These attractive and repulsive forces act on the approaching electrospun fiber which is guided just before its landing on the collector. Other studies proved that the intensity of the electric field resulting from the charges carried on the suspended fibers can be manipulated by modifying the geometry and the electrical properties of the patterned collector[11,25] as well as the processing parameters such as the voltage, the electrical properties of solvents[26–30] and ambient conditions such as the temperature and humidity.[31]

Nevertheless, because the charged nanofibers deposited during the first times modify the electric field at the vicinity of the collector top surface, the manner the nanofibers are deposited after longer time of production can be subjected to modification. As a consequence, a high level of control of the membrane 3D structuration during the time of its fabrication is difficult. On one hand, such phenomenon can be advantageously exploited as for example when the fabrication of membranes with gradient of pore size is targeted.[13] On the other hand, the well-controlled 3D structuration of membranes can be lost after only a short time of fiber deposition.[14] Such phenomena are due to the fact that the electrostatic template evolves, progressively or suddenly, during the membrane fabrication. Thus, the on-line measurement of the electrostatic template during electrospinning could be very interesting in order to track the deposition of the nanofiber and monitor the 3D structuration of the membrane. In a recent article, we demonstrated that, by simply using an electrostatic voltmeter, the on-line measurement of the surface potential located at the top surface of the deposited fibers gives useful information on the local morphology of the membrane during its fabrication such as the nanofiber diameter as well as the inter-fibers pore size.[32]

In the present article, we focus on the on-line measurement of the surface potential resulting from the electrostatic template induced by the deposition of electrospun nanofibers on patterned collectors. First, the case of the nanofiber deposited above a single gap is deeply investigated. To this end, electrospinning is carried out onto a cylindrical rotating collector having a single adjustable gap, while continuously measuring the surface potential during the process of electrospinning. Furthermore, a model is developed in order to get more insight into the kinetics of the surface potential generated from the suspended fibers as a function of the gap size and the polymer-solvent formulation. To this end, three polymer have been studied: poly(lactic acid) (PLA), poly(ethylene oxide) (PEO) and a blend of PEO and alginate (PEO-Alginate). A fourth system was also studied: PLA plus the addition of a salt. These polymers have been chosen because (i) they are used for many applications[33,34] and furthermore, (ii) their electric properties as well as those of their solutions are very different resulting to different kinds of surface potential behaviors. Finally, electrospinning using a complex micropatterned collector is studied. The surface potential kinetics is thus analyzed in correlation with the evolution of the 3D microstructuration of the mat during its fabrication.

2. Materials and methods

2.1 Materials and solution preparation

Poly(D,L-lactide) (PLA) (Ingeo 7000D, Natureworks, M_w = 180 kg/mol), PEO (M_w = 400 kg/mol, Sigma-Aldrich), benzyltriethylammonium chloride (TEBAC), sodium alginate (low viscosity of 4 to 12 mPa.s (cP) at 1% (w/w) in H_2O at 25 °C, Ref A1112, Sigma-Aldrich) and deionized water were used as received. Dichloromethane (DCM) and N, N-Dimethylformamide (DMF) were purchased from Sigma-Aldrich.

PLA solutions for electrospinning were prepared by dissolving PLA in DMF/DCM (50:50 v/v) to get a polymer weight concentration of 9% (w/w). TEBAC (0.5% w/w) was added to the PLA solution to get a PLA/TEBAC solution. Each solution was stirred magnetically overnight at room temperature in a glass bottle. With the same method, 5% w/w PEO in deionized water was stirred 24h prior to electrospinning. PEO-Alginate system was produced by adding 1% w/w alginate in the PEO solution.

2.2 Electrospinning process

A sketch of the experimental setup is shown in Figure 1. The single gap collector is made of two aluminum cylinders having each a width of 70 mm, a diameter D = 12 cm and separated by an air gap centered below the needle emitter. The gap g can be continuously adjusted from 0 to 10mm. The electrospun fibers were deposited on the grounded collector rotating at 120 RPM. It is worth noting that at this rotation speed, there is no fiber alignment induced by the collector rotation. Mechanical fiber alignment occurs at much higher rotation speed (and in fact at a much higher tangential velocity at the collector surface $V = R\Omega$, with R being the collector radius and Ω the rotation speed in $rad.s^{-1}$).It was shown that below 1000 RPM (at a tangential velocity of $V = 0.06 \times 1000\ \pi / 30 \sim 6.3\ m.s^{-1}$), there is no effect of the collector rotation speed. Thus, below 1000 RPM, the random whipping movements of the electrospun jet are much faster than the tangential velocity of the collector. Efficient mechanical fiber alignment was observed at tangential velocities greater than 10 $m.s^{-1}$.[35] In conclusion, the fiber alignment observed in all experiments of the present article was only induced by the Coulomb force resulting from the electric field between the patterned collector (gap or grid) and the charged electrospun jet.

The solutions were fed using a syringe pump (Fischer scientific) with a 24G stainless steel needle having an inner diameter of 0.5 mm. The needle was electrically connected to the positive terminal of a high voltage DC power supply (Spellman SL10). The distance between the tip of the needle and the surface of the collector was maintained constant at 15 cm. The electrospinning voltage was kept constant at 25 kV and the solution flow rate at 1 ml/h. The air in the electrospinning chamber was set to a temperature of 21 ± 1°C with a relative humidity of 38 ± 2 %.

To measure the surface potential, a non-contacting electrostatic voltmeter ESVM (Trek Model 347-3-H-CE) connected to a computer for data acquisition was used. The measurement is based on a field-nulling technique for non-contacting voltage measurement achieving direct current stability and high accuracy, with no need for fixed probe-to-surface spacing. The technique allows an accurate measurement of the surface potential of stationary or moving surfaces. The measurement range is 0 to ± 3 kV with an accuracy of 0.1% of the full range. The probe of the voltmeter (end-view probe model 6000B-7C with a speed of response of 4.5 ms for 1 kV step) having a disc surface of 11.2 mm diameter was placed 2 mm below the surface of the collector as shown in Figure 1. An acquisition rate of 30 measurements per second was chosen.

All experiments have been carried out with gaps smaller than 10 mm so as not to exceed the maximum value measurable by the sensor (*i.e.* 3 kV). Thus, for such configurations, the diameter of the sensor is larger than the gap and consequently the voltage V_{probe} measured by the ESVM probe and the actual average voltage above the gap covered by the suspended fibers $\bar{V}_{gap}$ are not identical. For this purpose, a model experiment was designed allowing to find the relationship between V_{probe} and $\bar{V}_{gap}$ (see section 1 of Supp. Info. for this purpose).

Experiments (see Figure S3 of Supp. Info) have been carried out to measure the total electric current i_{jet} corresponding to the flow of charges through the electrospun jet. For this purpose, the collector was connected to a secondary aluminum ring and the gap was set to g = 0 mm. A resistor R (R = 500 MΩ for PLA and 10 MΩ for PEO) was connected to one end to the secondary aluminum ring and its other end to the ground. The voltage U_R was measured on

the surface of the secondary aluminium ring using the ESVM probe. The current flowing through the resistor corresponds to the electrospun jet current $i_{jet} = U_R/R$. The current was constant during the time of electrospinning.

Finally, electrospinning of PLA on a micropatterned grid has been carried out. In this case, a rotating grounded cylindrical collector having a diameter of 60 mm and a width of 300 mm was used. A stainless steel grid with regular square patterns with a pitch of 250 µm has been placed against the cylindrical collector. The grid is a woven mesh and was purchased from Gantois industries, https://www.gantois.com/en/home.php. It is obtained by intertwining parallel tighten wrap wires and perpendicular weft wires. The mesh of the grid is a square with a nominal opening (relative distance between two wires) of 150 µm and the wires have a diameter of 100 µm. The rotation speed of the collector was set to 120 RPM. For the on-line measurement during electrospinning of the surface potential above the deposited fibers, the probe of the ESVM was placed 2 mm below the surface of the grid opposite to the needle emitter. An acquisition rate of 30 measurements per second was also chosen. All other parameters (formulation, process…) were kept the same as for the electrospinning of PLA on the collector with the adjustable single gap. The surface potential was also measured under the same conditions but without the grid.

2.3 SEM measurements

All samples were gold coated (sputter Quorum Q 150 RS, Quorum Technologies) for 2 min before SEM observation (Vega-3, Tescan). To study the aligned fibers, an aluminum sheet (40mm × 25mm) with a rectangular hole having a width corresponding to the studied gap of the collector is used to collect the suspended fibers. Each side of the aluminum sheet on both side of the rectangular hole is stuck on the metal part of the collector. The rectangle hole is centered on the collector gap, with the longer edge of the hole along the edge of the gap. Once the electrospinning process is completed, the aluminum sheet presenting suspended fibers over the rectangular hole is taken off from the collector. The fiber density was calculated from SEM images taken at 5 randomly chosen locations of the suspended fibers area.

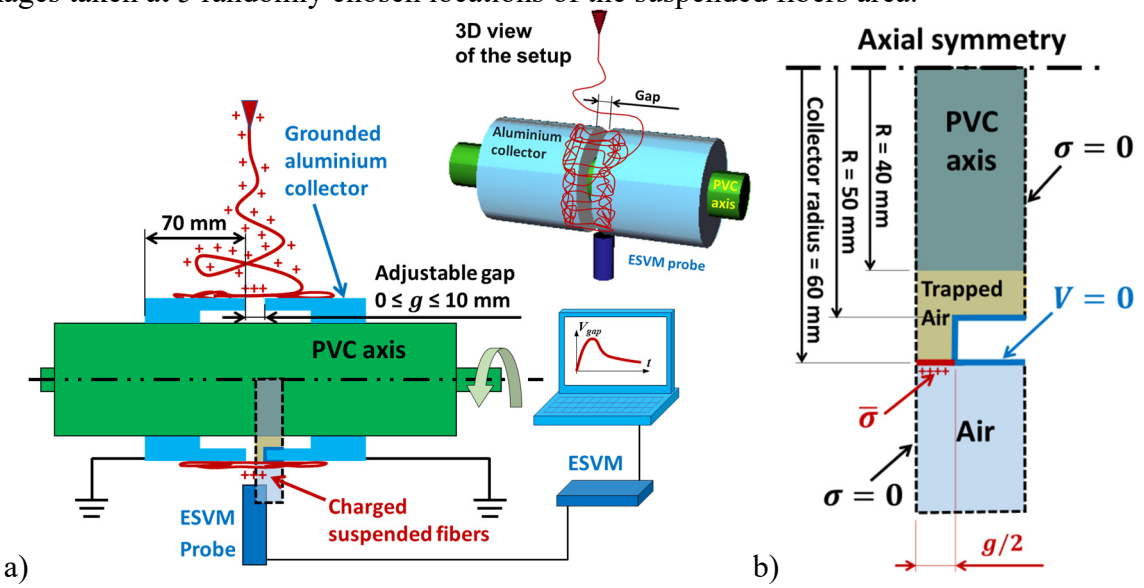

Figure 1. *a) 3D view and cross-section of the experimental setup for the measurement of the surface potential above the suspended fibers. b) Detail of the collector highlighted in a) allowing the calculation by the finite elements method of the electric field induced by the suspended fibers and the gap capacitance C_{gap} due to the trapped air below the suspended fibers. The surface charge density σ was set to 0 along all dotted lines and to $\bar{\sigma}$ above the suspended fibers.*

2.4 Numerical simulations

Numerical simulations using Comsol® software were carried out in order to calculate (i) the electric field located above the charged suspended fibers and (ii) the capacitance C_{gap} resulting from the trapped air between the vertical walls of the collector and the charged fiber strands. The numerical simulations were carried out on the geometry depicted in Figure 1b.

3. Results and discussion

First, electrospinning was carried out using a cylindrical collector without gap (i.e. g set at 0 mm) to measure the total electric current i_{jet} flowing towards the ground. A current i_{jet} of 142 ± 15 nA was measured in the case of PLA electrospun from DCM/DMF solutions whereas a value of 1900 ± 70 nA was obtained for PEO dissolved in water. Thus, much more charges are brought from the PEO jet compared to the PLA one. Figure 2a shows the evolution of the surface potential above the deposited fibers as a function of time for g = 0. Two regimes are observed in the case of PLA. Indeed, after a lag time of few tens of seconds during which the surface potential is almost equal to 0 V, a linear increase of the voltage is measured with a value reaching 250 V after 300 s of electrospinning. At the very beginning of production, the deposited fibers are in perfect contact with the collector allowing an efficient release of the charges towards the ground. However, after the lag time, the surface potential increases due to the increasing thickness of the deposited fibrous mesh providing electrical resistance with the production time.[32] This behavior is explained by the morphology of the porous mat. Indeed, each pore of the fibrous mat can be modeled by a fully charged R_pC_p circuit where the capacitor C_p is formed by the air trapped in the pore (the dielectric medium of the capacitor) surrounded by the charged fiber strands (the electrodes of the capacitor) and the resistance R_p is related to the fiber-fiber electric contact quality and the resistivity of the polymer.[32] Because, the capacitor is fully charged during electrospinning, the R_pC_p circuit behaves as a simple ohmic circuit of resistance R_p. Thus, increasing the resistance value leads to the raise of the surface potential in the same proportion. However, in the case of PEO, it is shown that the surface potential remains equal to 0 V, even though the measured current is much higher than for PLA. Such a result demonstrates that PEO fibers release their charges very quickly. In this case, the R_p value of each pore behaves as a short-circuit avoiding the increase of the surface potential.

The evolution of the surface potential generated by suspended fibers above a gap g of 3 mm is also shown in Figure 2a. SEM pictures of suspended PLA and PEO fibers can also be seen in Figure 2c-d. As expected, it is shown that after a short time of electrospinning (i.e. t = 30 s) fibers are mostly aligned perpendicularly to the gap[26] with a better alignment in the case of PLA fibers. For longer time of electrospinning, the fibers alignment is eventually lost. In the case of PLA, a dramatic increase of the surface potential is observed immediately after switching on the power supply connected to the emitter (*i.e.* the needle). In less than 15 s, the average surface potential reaches a peak of 2200 V. Then, the voltage decreases during around 20 s before reaching a plateau at 1500 V. It is also shown that the surface potential fluctuates a lot with a disparity of ± 200 V around the average value. These fluctuations, which are much greater than what was measured when the gap was set to 0 mm, may be caused by uneven suspended fibers deposited above the gap inducing a non-uniform electric field. In the case of PEO fibers, the evolution of the surface potential can also be divided in three stages: (i) a rapid increase followed by (ii) a decrease and then (iii) a plateau regime. However, the kinetics is slower than what it is observed for PLA. Indeed, although a much higher amount of charges is carried by the PEO jet, the surface potential reaches only a maximum value of 300 V which is 7 times lower than what was measured for PLA. Thus, the charges brought by the electrospun jet are dissipated much faster in the case of PEO than for PLA. This behavior might be due to residual water remaining in the fibers leading to a low electric resistance of the PEO fibrous

mesh favoring the charge dissipation and consequently the decrease of the surface potential. As the evolution of the surface potential should be linked to the amount of charges and thus the amount of deposited suspended fibers, the density of deposited suspended fiber strands $\rho_g(t)$was calculated. This density $\rho_g(t)$, obtained from SEM measurements, is defined as the ratio between the total length of deposited suspended fiber strands $L_g(t)$ and the surface of the gap $S_{gap} = \pi Dg$:

$$\rho_g(t) = \frac{L_g(t)}{\pi Dg} \quad (1)$$

The time evolution of the surface potential and the density ρ_g is shown in Figure 2b for PLA with a gap of 3 mm and for PEO with a gap of 7 mm. In both cases, a regular increase of $\rho_g(t)$ is observed during the production time. Thus, although the fibers are uniformly deposited over the gap, the surface potential is subjected to a complex non-linear behavior which cannot only be explained by the amount of charges brought by the deposited fibers. The way the deposited fiber strands release their charges seems to play an important role. Thus, in order to get more insight into such phenomena, a model was built to interpret the surface potential kinetics.

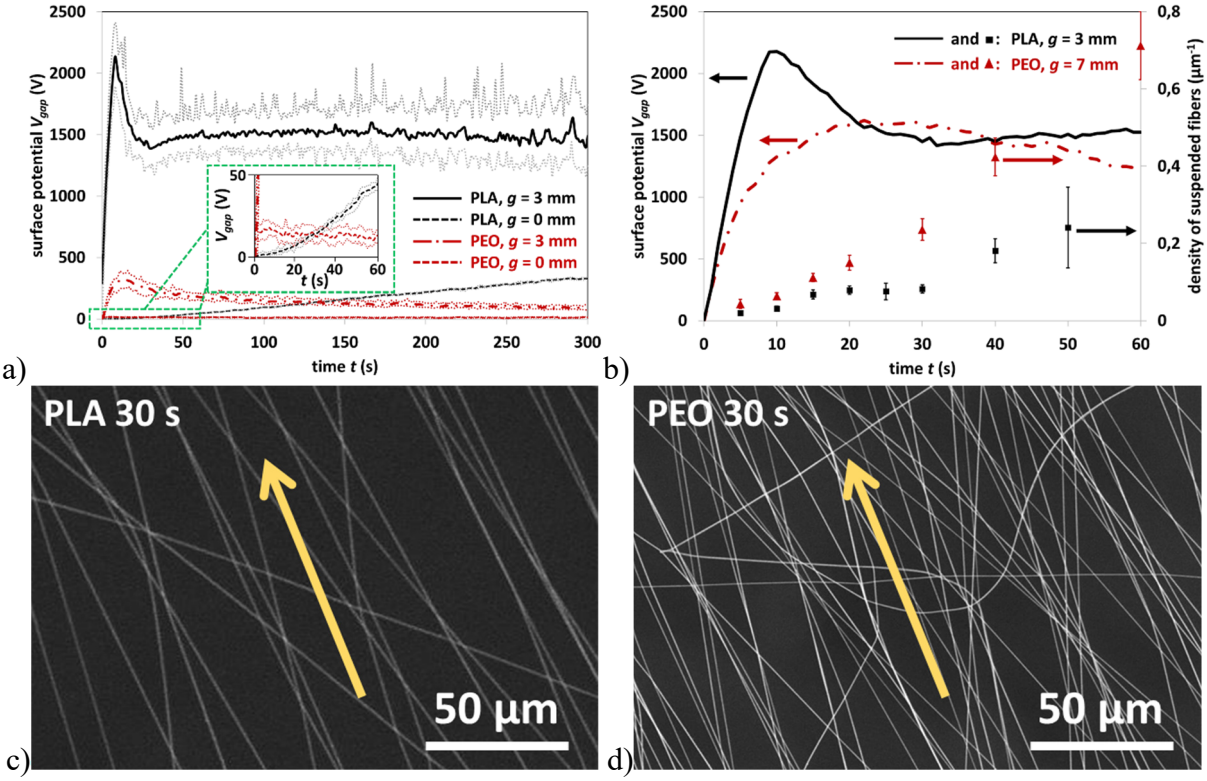

Figure 2. *a) Surface potential during electrospinning of PLA (black) and PEO (red) for gaps of 3 mm and 0 mm. The bold lines represent the average of the surface potential and the thin dashed lines represent the envelop curves highlighting the maximum and minimum values measured during the experiments. b) Surface potential and density of deposited fiber strands ρ_g as a function of time for PLA with a gap g = 3 mm (black) and PEO with a gap g = 7 mm (red). c) SEM picture of suspended PLA fibers and of d) suspended PEO fibers after 30 s of electrospinning.*

3.1. Surface potential kinetics above a single gap during electrospinning: a model

3.1.1. The case of suspended parallel and non-interacting fiber strands

A first model is proposed assuming that the suspended fiber strands are perfectly perpendicular to the gap and consequently do not interact with each other. Once deposited, the N^{th} fiber strand immediately starts to release its charges from its central part where the potential reaches a maximum value towards its grounded ends. Indeed, the charges located along the strand induce a local potential being maximum around the central part of the gap and equal to 0 V at the fiber-collector contact point (Figure 3a). The resulting potential difference generated along the suspended fiber strand induces a charge release towards the collector. Furthermore, the air pocket trapped between the vertical walls of the collector and the fiber strands can be seen as the dielectric material of a charged capacitor C_{gap} whereas the fiber strand behaves as a wire of resistance *R* allowing the flowing of the charges towards the metallic walls of the collector. Thus, a charged fiber strand *i* located over an air gap with its ends connected to the ground can be considered as an RC circuit having a characteristic time $\tau = RC$. Once deposited, it immediately starts to release its charges. Thus, for a given time *t*, the amount of charges carried by the i^{th} fiber strand $q_i(t)$ is:

$$q_i(t) = q_0 e^{-(t-t_i)/\tau} \tag{2}$$

Where t_i is the time corresponding to the deposition of the i^{th} fiber strand on the gap collector and q_0 is its amount of initial charges:

$$q_0 = \lambda g \tag{3}$$

Where λ is the linear charge density of the electrospun jet just before it comes into contact with the surface of the collector and g is the gap size. If one considers that a fiber strand *i* is deposited over the gap every Δt, then its amount of charges at time *t* is given by:

$$q_i(t) = q_0 e^{-(N-i)\Delta t/\tau} \tag{4}$$

Therefore, the total amount of charges $Q(t)$ induced by *N* strands is:

$$Q(t) = \sum_{i=1}^{N} q_i = \sum_{i=1}^{N} \lambda g e^{-(N-i)\Delta t/\tau} = \lambda g \sum_{j=0}^{N-1} e^{-j\Delta t/\tau} \tag{5}$$

The average surface charge density $\bar{\sigma}(t) = Q(t)/\pi D g$ is then:

$$\bar{\sigma}(t) = \frac{\lambda}{\pi D} \sum_{j=0}^{N-1} e^{-j\Delta t/\tau} = \frac{\lambda}{\pi D} \frac{1-e^{-N\Delta t/\tau}}{1-e^{-\Delta t/\tau}} \tag{6}$$

Because $t = N\Delta t$ and assuming that $\Delta t \ll \tau$, one obtains the average surface charge density as a function of time:

$$\bar{\sigma}(t) = \frac{\lambda}{\pi D} \frac{\tau}{\Delta t} \left(1 - e^{-t/\tau}\right) \tag{7}$$

Numerical simulations based on the finite elements method (see section 4 and Figures S6 and S7 of Supp. Info. for more details) have made it possible to obtain the relationship between the average surface potential $\bar{V}_{gap}(t)$ above the fibrous surface of the suspended fibers and $\bar{\sigma}(t)$:

$$\bar{V}_{gap}(t) = k \frac{g}{\varepsilon_0} \bar{\sigma}(t) \tag{8}$$

Where ε_0 is the permittivity of air and k is a form factor depending on the collector diameter. The trapped air below the suspended fiber strands can be seen as a capacitor C_{gap} having a capacitance such as $C_{gap} = Q/\bar{V}_{gap} = \pi D g \bar{\sigma}(t)/\bar{V}_{gap}$. Thus, by identification one obtains:

$$C_{gap} = \frac{\pi D \varepsilon_0}{k} \quad (9)$$

The numerical simulations show that $\bar{V}_{gap}$ does not depend on the collector diameter (see Figure S7a in Supp. Info.) and mostly corresponds to the asymptote value when $D \to \infty$ (*i.e.* plane situation). Thus, a value of $k \cong 0.16$ was obtained (see Figure S7b in Supp. Info.) whatever the gap value and a capacitance $C_{gap} \cong 2.1\ 10^{-11}$ F is calculated for a collector diameter $D = 120$ mm. If one introduces i_g, the rate of deposited charges over the gap, as the amount of charges deposited over the gap per unit time and corresponding to a fraction β of the total current i_{jet} coming from the jet, it leads to:

$$i_g = \frac{\lambda g}{\Delta t} = \beta i_{jet} \quad (10)$$

Finally, from equations 7-10, the average potential located above the suspended fiber strands is given by:

$$\bar{V}_{gap}(t) = \frac{i_g}{C_{gap}} \tau \left(1 - e^{-t/\tau}\right) \quad (11)$$

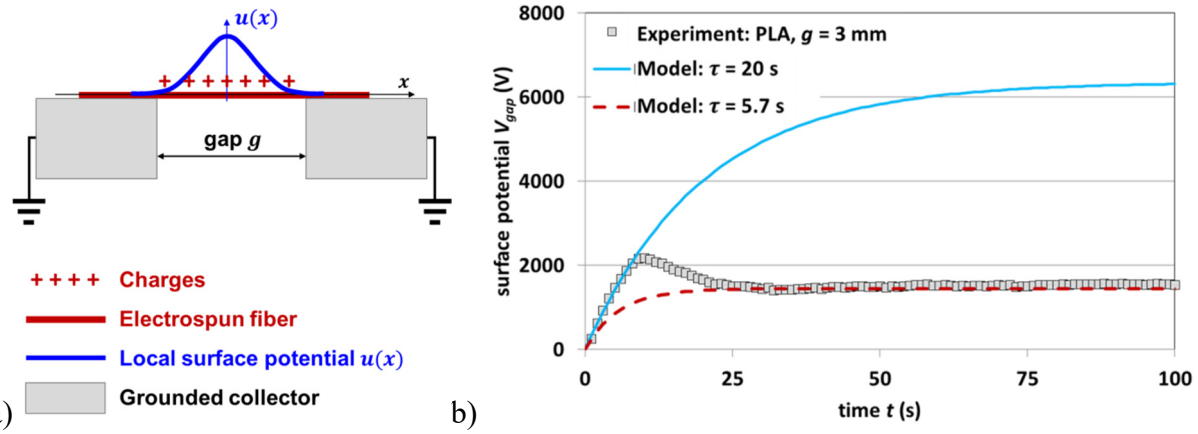

Figure 3. *a) Local surface potential induced by a charged suspended fiber strand connected at its extremities to the grounded collector. b) Surface potential of suspended PLA fiber strands with a gap of 3 mm. Experimental points (black squares), model from equation 11 with τ = 20 s (solid blue line) model from equation 11 with τ = 5.7 s (dashed red line).*

When $t \ll \tau$, equation 11 shows that, at the beginning of electrospinning, the surface potential evolves linearly with time which can be easily explained by the fact that each deposited fiber strand brings its own charges which do not have the time to be released. Thus, at short times (*i.e.* $t \ll \tau$), the initial slope of the surface potential gives the rate of deposited charges i_g :

$$\frac{d\bar{V}_{gap}}{dt}(t \ll \tau) \approx \frac{i_g}{C_{gap}} \quad (12)$$

When $t \gg \tau$, equation 11 shows that the surface potential tends to an asymptote:

$$\bar{V}_{gap}(t \gg \tau) \approx \bar{V}_{\infty} = \frac{i_g}{C_{gap}} \tau \quad (13)$$

Using equations 12 and 13, an estimation of i_g and τ can be done with:

$g = 3$ mm, $\frac{d\bar{V}_{gap}}{dt} = 250$ Vs^{-1}, $C_{gap} = 2.1\ 10^{-11}$ F and $\bar{V}_{\infty} = 1422$ V

One obtains:

$i_g = 5.25$ nA and $\tau = 5.7$ s

From Figure 3b, it is shown that taking τ = 5.7 s, the model cannot fit the first and the second stage of the experimental curve. If we try to fit the first stage, a much greater τ value must be considered (τ = 20 s), but in this case $\bar{V}_\infty \approx 6350$ V! Thus, it appears that the characteristic time τ related to the kinetics of charge release along the suspended fiber strands should decrease during the first times of deposition. For this purpose, another model is proposed.

3.1.2. The case of interacting suspended fiber strands

Figure 4a shows a sketch of the collector during electrospinning with suspended fiber strands crossing each other over the gap. Indeed, a close view shows that the suspended fiber strands interact with each other forming closed loops (highlighted in white in Figure 4b) equivalent to resistor-capacitor circuits of resistance R_{loop} and capacitance C_{loop} (Figure 4c). The thin deposited layer of fiber strands can be seen as the association of a large number of RC circuits having an equivalent resistance $R(t)$ and a capacitance C_{gap}(Figure 4d). Because the size of the loops decreases during electrospinning (Figure 4e-g), it is expected that $R(t)$ follows the same tendency. However, as already mentioned, C_{gap} characterizes the capacitance of the trapped air pocket between the walls of the collector and the suspended fibrous layer (Figure 1b), it is thus a constant during the time of electrospinning. The characteristic time of the charged suspended fibrous layer can thus be written as follows:

$$\tau(t) = R(t)C_{gap} \tag{14}$$

Using equation 9, the characteristic time can also be written as:

$$\tau(t) = \frac{\pi D \varepsilon_0}{k} R(t) \tag{15}$$

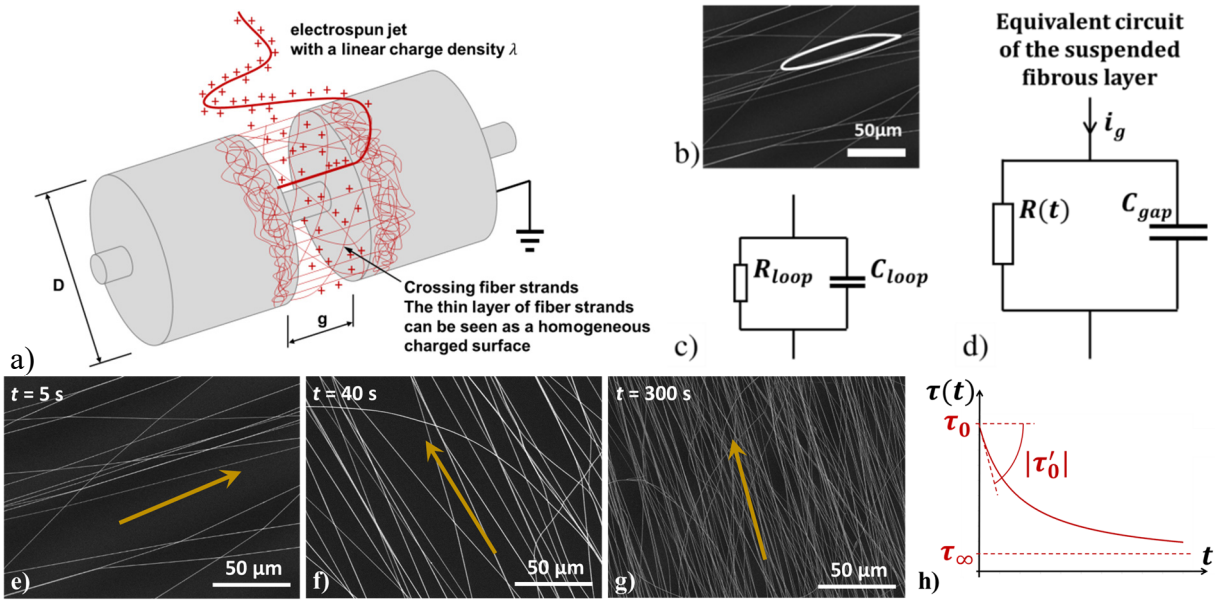

Figure 4. *Model taking into account interacting fiber strands. a) Sketch of the set-up with a fiber being deposited above the gap. b) SEM showing PLA crossing fibers forming a closed loop highlighted in white. c) Each loop can be seen as a short RC circuit. d) Equivalent circuit of the thin suspended fibrous layer. PLA fiber strands suspended over a gap of 3 mm after e) 5 s, f) 40 s and g) 300 s. h) Graph of the proposed behavior of the characteristic time versus time.*

Thus, the suspended fibrous layer is equivalent to an RC circuit through which a current i_g flows as shown in Figure 4d. The behavior of such circuit is characterized by the following differential equation:

$$\frac{d\bar{V}_{gap}}{dt} + \frac{\bar{V}_{gap}}{\tau(t)} = \frac{i_g}{C_{gap}} \tag{16}$$

Equation 16 cannot be solved directly due to the fact that the characteristic time is not a constant. It can be noticed that if $\tau(t)$ was a constant, then the solution would be equivalent to equation 11 corresponding to non-interacting fiber strands. The form of the function $\tau(t)$ must be proposed in order to solve equation 16. As previously hypothesized, the characteristic time $\tau(t)$, and consequently the resistance $R(t)$, must decrease during electrospinning due to the decrease of the size of the loops (Figure 4e-g). The following empiric equation is thus proposed:

$$\tau(t) = \tau_\infty + \frac{(\tau_0 - \tau_\infty)^2}{|\tau_0'|t + \tau_0 - \tau_\infty} \tag{17}$$

Where $\tau_0 = \tau(t = 0)$, τ_∞ is the asymptote of $\tau(t)$ and $|\tau_0'|$ is the absolute value of the initial slope (see Figure 4h). Using equation 17, it is possible to solve the differential equation 16. After integration and imposing the initial conditions, the complete solution is:

$$\bar{V}_{gap}(t) = K(t)G(t) \tag{18}$$

$$G(t) = [\tau_\infty|\tau_0'|t + \tau_0(\tau_0 - \tau_\infty)]^\gamma e^{-t/\tau_\infty} \tag{19}$$

$$K(t) = \frac{i_g}{C_{gap}} \int_0^t [\tau_\infty|\tau_0'|t' + \tau_0(\tau_0 - \tau_\infty)]^{-\gamma} e^{t'/\tau_\infty} dt' \tag{20}$$

$$\gamma = \frac{(\tau_0 - \tau_\infty)^2}{\tau_\infty^2|\tau_0'|} \tag{21}$$

The integral in equation 20 can be numerically estimated using a Simpson method. In order to avoid any numerical divergence when calculating $\bar{V}_{gap}(t)$ in the case of large values of γ exponent, $G(t)$ is placed inside the integral of $K(t)$. In the following, equation 18-21 are used to model the surface potential in various situations.

3.2. Evolution of the surface potential as a function of the gap and the polymer solution

Figure 5a-b show experiments and their modeling of the time evolution of the surface potential $\bar{V}_{gap}(t)$ as a function of the gap size for PLA and PEO suspended fibers respectively. Due to the range of the electrostatic voltmeter, the tested gap size was set between 0.5 mm and 3 mm in the case of PLA and between 1 mm and 10 mm for PEO. Whatever the gap value, the kinetics of the surface potential can be divided in three distinct stages: a sharp increase at the first moments followed by a decrease before reaching a plateau. However, smoother variations can be observed for PEO than for PLA.

Regarding the first stage of $\bar{V}_{gap}(t)$, the surface potential increases sharply and almost linearly as a function of time. Knowing that the density of deposited suspended fiber strands $\rho_g(t)$ can be obtained experimentally at the beginning of electrospinning (see equation 1 and Figure 2b), it is possible to calculate the rate of deposited suspended fiber strands $\dot{\rho}_g$ as follows:

$$\dot{\rho}_g = \frac{d\rho_g}{dt} = \frac{1}{\pi D g}\frac{dL_g(t)}{dt} \tag{22}$$

Thus, from the model it can be seen that at the very beginning of the electrospinning (*i.e.* when very few interactions occur between the deposited fiber strands over the gap), the surface potential scales as:

$$\bar{V}_{gap}(t \to 0) \sim \frac{i_g}{C_{gap}} t = \lambda \dot{\rho}_g k \frac{g}{\varepsilon_0} t \tag{23}$$

Equation 23 is well verified as the current i_g increases almost linearly with the gap as shown in Figure 5c-d. It is recalled that the capacitance C_{gap} does not depend on the gap size (see equation 9). Thus, at the very first moments, the larger the gap, the larger the current i_g, which shows that in the studied range of gaps, the rate $\dot{\rho}_g$ is constant.

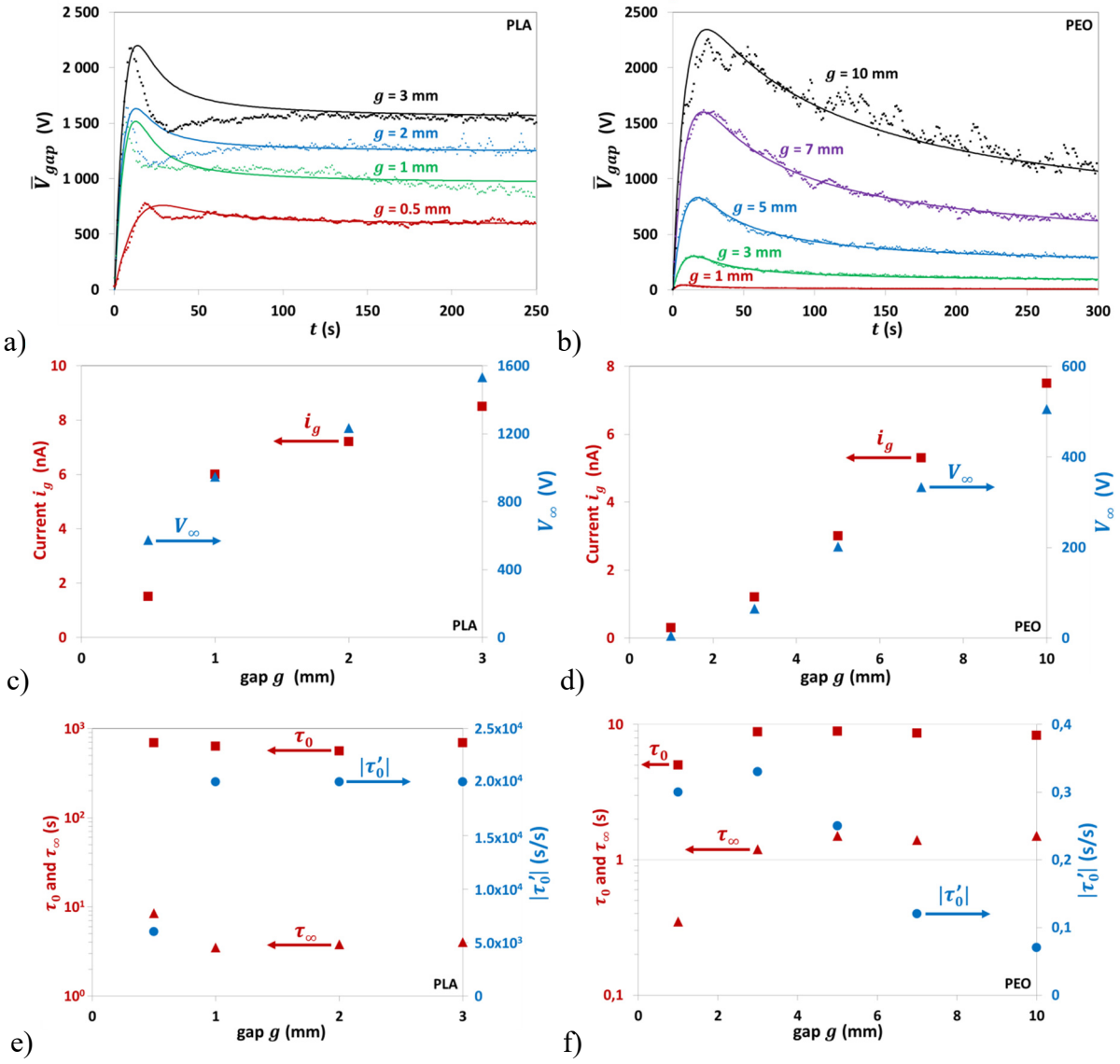

Figure 5. *Experimental results (points) and model (solid lines) of the surface potential as a function of time for various gaps in the case of a) PLA and b) PEO. Current i_g (red squares) and potential V_∞ (blue triangles) as a function of the gap for c) PLA and d) PEO. τ_0 (red squares), τ_∞ (red triangles) and $|\tau_0'|$ (blue discus) as a function of the gap for e) PLA and f) PEO.*

During the second stage, the surface potential $\bar{V}_{gap}(t)$ decreases sharply with time. The decrease of the surface potential is explained by the fact that the characteristic time decreases as a function of time (i.e. $|\tau_0'|$ has a significant effect on the kinetics of the surface potential) due to the interactions between the fiber strands decreasing the overall resistance $R(t)$ of the suspended fibrous layer. Moreover, in the case of PEO, it is seen that $|\tau_0'|$ decreases with the gap which means that the second stage of $\bar{V}_{gap}(t)$ gets smoother when increasing the gap.

Whereas the third stage is reached very rapidly (*i.e.* after only 30s) in the case of PLA, the plateau value $\bar{V}_\infty$ is only reached after 240 s for g = 7 mm and hardly ever reached after 300 s for g = 10 mm in the case of PEO. Moreover, it is observed that the time to reach the surface potential plateau increases with the gap, as predicted by the model showing that $\bar{V}_\infty$ scales as:

$$\bar{V}_{gap}(t \to \infty) = \bar{V}_\infty = \lambda \dot{\rho}_g k \frac{g}{\varepsilon_0} \tau_\infty = \frac{i_g}{C_{gap}} \tau_\infty \quad (24)$$

Finally, it is observed that the gap has no significant effect on τ_0 and τ_∞ (see Figure 5e-f). Such behavior shows that the initial and final behavior of $\bar{V}_{gap}(t)$ is mostly governed by the initial and final fibrous morphology of the suspended fiber strands. Indeed, whatever the gap value (except in the case of g = 0.5 mm for PLA), the fiber strands are mostly parallel to each other at the very first moments of electrospinning. For the longest studied times, when the plateau is reached, the size of the fibrous loops (see Figure 4b) reaches a minimum value corresponding to a minimum value of the average resistance $R(t)$ of the fibrous layer suspended above the gap.

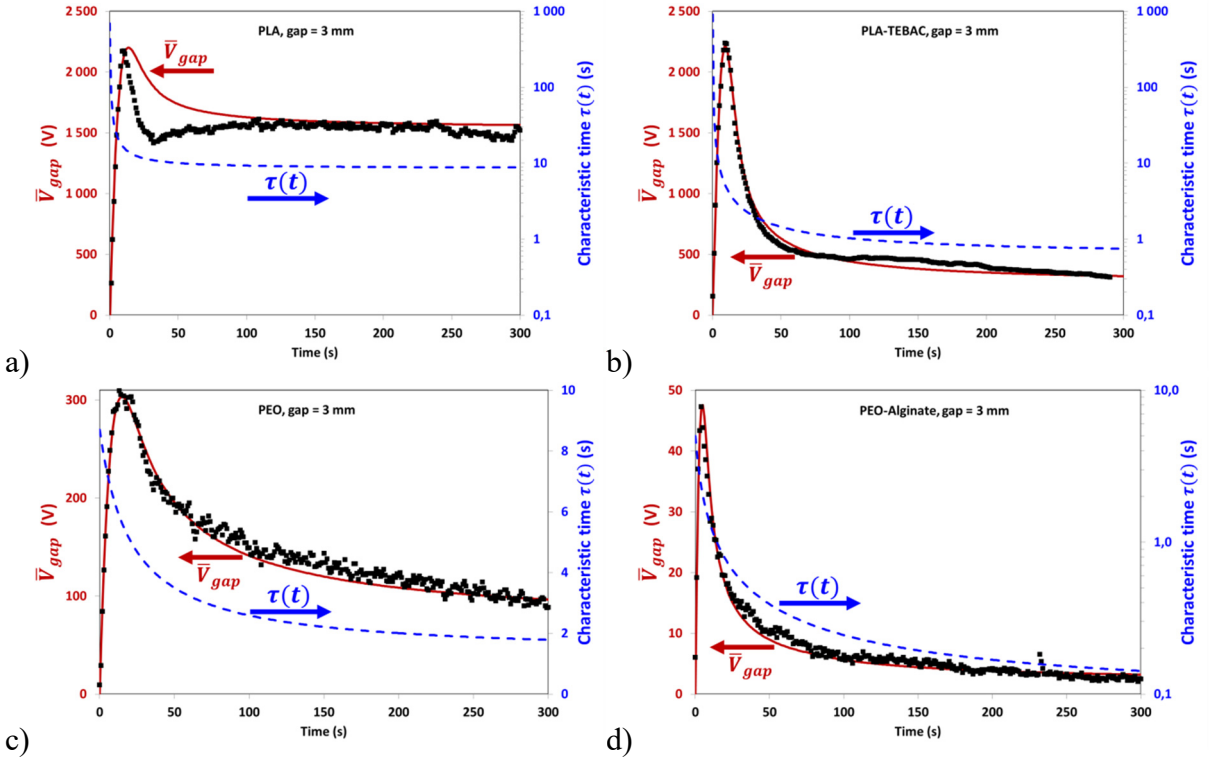

Figure 6. *Behavior of various systems with a gap = 3 mm. Surface potential (black squares: experimental result, red lines: model from equation 18-21) and the characteristic time $\tau(t)$ (blue dashed line) as a function of time. a) PLA. b) PLA-TEBAC. c) PEO. d) PEO-Alginate.*

Figure 6 (see also Figure S4 in the Supp. Info. to compare the curves on a single graph) shows experiments and their modeling of the time evolution of the surface potential measured for various polymer systems electrospun under the same conditions and with a gap of 3 mm. It is seen that the model taking into account the interactions between the fiber strands allows an excellent fitting of experimental curves. As for PLA and PEO, it is shown that the surface potential $\bar{V}_{gap}$ of PLA-TEBAC and PEO-Alginate suspended fiber strands follow a similar trend with three successive steps. Indeed, both systems are firstly subjected to a sharp linear increase of $\bar{V}_{gap}$ before reaching a peak value and then decreasing to an asymptotic value V_∞. For each electrospun polymer solution, table 1 gives the parameters τ_0, τ_∞ and $|\tau_0'|$ allowing the best fitting. In all the cases, the characteristic time decreases during electrospinning before

reaching an asymptotic value τ_∞ corresponding to a stabilized fibrous morphology over the gap. Indeed, the size of the loops formed by the crossing fiber strands decreases gradually during electrospinning resulting in the decline of $R(t)$. After a long time of electrospinning, the size of the loops reaches a critical value related to the fiber diameter [36] leading to a constant $R(t)$ and therefore a constant characteristic time $\tau(t) \sim \tau_\infty$.

In the case of PLA-TEBAC fibers, it can be noticed that the kinetics of the surface potential is almost the same as for pure PLA fibers regarding the first step and the beginning of the second one as shown in Figure S4 and as characterized by the model parameters influencing the two first steps of the surface potential, *i.e.* i_g, τ_0 and $|\tau_0'|$. The low amount of TEBAC salt introduced in the formulation didn't allow to enhance significantly the amount of charges characterized by i_g. Furthermore, TEBAC salt is not perfectly dispersed in the PLA matrix: domains of fibers are free of TEBAC.[32] Thus, at the beginning of electrospinning, the percolation threshold of TEBAC is not reached inside the large loops formed by the interconnected suspended fiber strands: the resistance $R(t)$ is similar to that of pure PLA fibers. However, after a longer time of electrospinning in the order of 25 s, as the size of the loops decreased, the percolation threshold of TEBAC may be suddenly reached explaining the low value of τ_∞ (*i.e.* 0.61 s) compared to that of pure PLA fibers (*i.e.* 4 s).

Table 1. *Parameters obtained for the fitting for g = 3 mm.*

	PLA	PLA-TEBAC	PEO	PEO-Alginate
i_g (nA)	8.5	9.5	1.2	0.5
τ_0 (s)	690	1450	8.8	5
τ_∞ (s)	4	0.61	1.2	0.089
$\|\tau_0'\|$ (s/s)	20000	50000	0.33	1.5
V_∞ (V)	1533	260	64.7	2

As previously mentioned, electrospinning of PEO induced a similar evolution of $\bar{V}_{gap}$ as a function of time than PLA but with smoother transitions between the three stages as well as with lower surface potential values. The surface potential decrease is even more pronounced in the case of PEO-Alginate system. Whereas τ_0 holds a high value of 690s in the case of PLA, the initial relaxation time reaches only a value of τ_0 = 8.8 s for PEO fibers and τ_0 = 5 s in the case of PEO-Alginate. As mentioned in equation 14, the relaxation time is the product of the capacitance C_{gap} induced by the trapped air below the suspended fibrous layer and the equivalent resistance $R(t)$ of the suspended fibrous layer. Because C_{gap}, given by equation 9, is related to the gap geometry alone, the decrease of $\tau(t)$ can only be explained by the variation of $R(t)$ which itself depends on the nature of the polymer, the possible content of residual solvents used for electrospinning and the quality of the fiber-fiber contact points. Furthermore, it is shown that PEO and PEO-Alginate fibers are subjected to slow variations of $\tau(t)$ as demonstrated by the low $|\tau_0'|$ values. Thus, the overall low resistance $R(t)$ estimated in the cases of PEO and PEO-Alginate systems is mainly explained by the higher fiber conductivity, as compared to PLA, allowing a faster charge release from the suspended fibers to the grounded collector. Indeed, whereas the conductivity of PLA is in the order of 2.10^{-18} S.cm^{-1},[37] the conductivity of pure PEO at room temperature is 10^{-9} S.cm^{-1},[38,39] a value which should be much more higher in the case of PEO-Alginate fibers due to the polyanionic character of alginate.

In the cases of PEO and PEO-Alginate, it is worth noting that the model leads to very low charge deposition rates, characterized by the current i_g. Indeed, when compared to PLA for which i_g = 8.5 nA, i_g reaches respectively only 1.2 nA and 0.5 nA for PEO and PEO-Alginate. At first glance, this estimation seems to be in contradiction with the fact that the total current

i_{jet}, corresponding to all the charges carried by the electrospun jet, is 13 times higher for PEO (i.e. 1900 ± 70 nA) than for PLA (i.e. 142 ± 15 nA). From equation 22 it is possible to calculate the rate of deposited suspended fiber strands $\dot{\rho}_g$ as follows:

$$\dot{\rho}_g = \frac{\alpha v_f}{\pi D g} \tag{25}$$

Where v_f is the electrospun fiber velocity and $\alpha = \frac{L_g(t)}{L(t)}$ is the fraction of fiber length which is deposited above the gap compared to the total deposited fiber length. The velocity of the jet can be easily estimated from the mass balance:

$$v_f = \frac{4 Q_{sol} \rho_{sol} C_{pol}}{\rho_{pol} \pi \phi_f^2} \tag{26}$$

Where Q_{sol} is the volume flow rate of the polymer solution, C_{pol} the weight polymer fraction in the solution, ρ_{sol} the density of the solution, ρ_{pol} the density of the polymer and ϕ_f the average fiber diameter. Thus, the fraction α of fiber strands deposited over the gap relative to the total deposited fiber length can be experimentally obtained:

$$\alpha = \frac{\dot{\rho}_g \pi^2 D g \rho_{pol} \phi_f^2}{4 Q_{sol} \rho_{sol} C_{pol}} \tag{27}$$

The fraction α is expected to be of the same order of magnitude as the fraction β obtained from the measurement of the currents i_g and i_{jet} as defined in equation 10. As shown in Table 2 for the case of PLA, β/α = 1.2 showing that the fraction of fibers deposited over the gap relative to the total fiber production corresponds to the fraction of charges deposited per unit time relative to all the charges brought by the electrospun jet. However, a huge discrepancy between α and β is observed in the case of PEO where β is 18 times lower than α. Such a discrepancy comes from the fact that the measured current i_g appears to be underestimated while the total current i_{jet} is high, as water is used as solvent. The only explanation of such an effect is that a fraction of $1 - \frac{\beta}{\alpha} \approx 94\%$ of the total charges brought by the suspended fiber strands at the time of their deposition is instantly dissipated and therefore, cannot be measured by the electrostatic voltmeter, which is only able to measure the surface potential after half a turn of the rotating collector.

Table 2. *Parameters used for the calculation of the fraction α of suspended fiber strands relative to the total produced fibers and fraction β being the ratio of the obtained i_g current to the total electrospun current i_{jet}.*

	g (mm)	$\dot{\rho}_g$ ($m^{-1}.s^{-1}$)	ρ_{pol} ($kg.m^{-3}$)	ϕ_f (nm)	Q_{sol} ($mL.h^{-1}$)	ρ_{sol} ($kg.m^{-3}$)	C_{pol} (%w/w)	α (%)	i_g (nA)	i_{jet} (nA)	β (%)	β/α
PLA	3	4166	1300	545	1	1150	9	5.0	8.5	142	6.0	1.2
PEO	7	10300	1125	169	1	1005	5	4.9	5.3	1900	0.3	0.06

Electrospinning over a gap is often expected to favor the fiber alignment perpendicular to the gap direction.[26] Indeed, in the case of PLA, an efficient fiber alignment was achieved as observed in Figure 4e-g. The degree of alignment was estimated from the analyses of SEM pictures giving the distribution of angle θ between the fiber directions and the direction perpendicular to the gap (Figure S8a). An angle θ = 0° corresponds to the expected and perfect fiber alignment. A standard deviation of 12° was obtained from SEM pictures taken in the case of fibers deposited after 50 s of electrospinning (Figure S8b). In the case of PEO electrospun during the same time (Figure S8c), a standard deviation of 23° was achieved which corresponds to lower fiber alignment than what was observed for PLA. When PEO-Alginate are electrospun a random fiber deposition is observed over the gap (Figure S8d). Such differences in the degree of fiber alignment can be explained from the different strength of the interactions between the surface potential and the charged upcoming jet in the three cases. Indeed, whereas a surface potential of ~ 1500 V was measured after 50 s of PLA electrospinning, the value reached 270 V for PEO and is lower than 10 V in the case of PEO-Alginate. Because at the upper vicinity of the gap the electric field is mainly induced by the surface potential,[14] lower Coulomb force, and thus poor fiber alignment, is experienced for PEO and even no alignment for PEO-Alginate. In the case of PLA, the surface potential $\bar{V}_{gap}$ (Figure 7a) and the degree of alignment characterized by the standard deviation of angle θ (Figure 7b) were plotted as a function of time for a long duration of electrospinning. It can be shown that at the very first moment (i.e. stage 1, when the surface potential increases rapidly and linearly with time) the fiber alignment is generally very poor (Figure 4e and S9a). This effect can be explained by the fact that during the first seconds of deposition, the electrospun jet is not subjected to a surface potential that could promote the electrostatic template effect responsible of the fiber alignment. Then, during several hundreds of seconds, a high degree of alignment characterized by a standard deviation of θ ~ 10 to 12°can be observed (Figure 7b and Figure 2c, 4f-g and S8b for SEM pictures). This stage is also characterized by a shoulder and a slight decrease of the surface potential up to 1900 s of electrospinning (stage 2 in Figure 7a). Finally, for long times of electrospinning (*i.e.* 5400 s), the degree of alignment is much less good (SEM in Figure S9b) with a standard deviation of θ ~ 31°. This loss of alignment may be related to the fact that as the thickness of the deposited fibers over the gap starts to be large compared to what it is deposited on the metallic edge which may hide the electrostatic template effect induced by the gap geometry. This result is in line with the slight increase of the surface potential observed between 1900 s and 5400 s (stage 3 in Figure 7a) which can be attributed to a higher accumulation rate of fibers over the gap (due to the loss of the electrostatic template effect) leading to charge accumulation as observed for standard non-woven electrospun mat.[32]

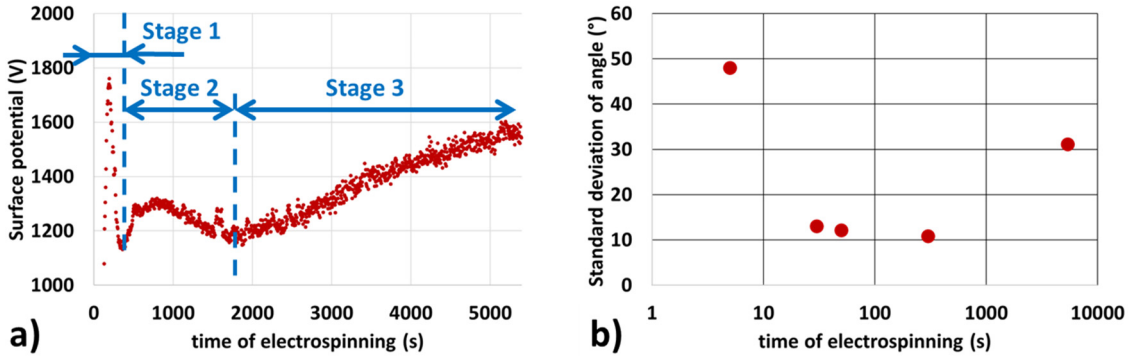

Figure 7. *Electrospinning of PLA over a gap of 3 mm. a) Evolution of the surface potential $\bar{V}_{gap}$ during electrospinning. Here, the very first points corresponding to the sharp initial increase of $\bar{V}_{gap}$ are not shown in order to zoom between 1000 V and 2000 V and show the slight increase of $\bar{V}_{gap}$ during the stage between 1900 s and 5400 s. b) Standard deviation obtained from the SEM image analyses of angle θ between the fiber direction and the one perpendicular to the gap as a function of the time of electrospinning.*

The on-line measurement of the surface potential throughout electrospinning is therefore a very valuable tool for the controlled fabrication of mats with aligned fibers which find a wide field of applications. Indeed, it has been shown that mats composed aligned fibers can be very attractive for various biomedical applications in order to mimic tissues such as tendon, heart or nerve.[40] In most of these applications, the mats must be only composed of aligned fibers for which the best fabrication technique is the mechanical alignment induced by depositing the fibers on a drum rotating at very high velocity. Indeed, the quality of the mechanical fiber alignment does not depend on the surface potential and thus the type of polymer-solvent which is electrospun. However, some applications require more complex aligned fibrous structures. This is for example the case of biomimetic scaffolds dedicated to the surgical reparation of tendon-to-bone area which need a gradation in terms of fibrous structure from aligned to random organization.[41] In this case, the use of a gap collector allows a one-step fabrication of such graded scaffolds with aligned fibers (i.e. those deposited over the gap) and randomly deposited fibers (i.e. those deposited on the metal edges of the collector). Because a high level of alignment is a key parameter to mimic the tendon zone, it is important to maintain the electrostatic template induced by the surface potential over the gap during all the process of electrospinning. Consequently, polyesters such as PLA or their derivatives are good candidates as they can be generally electrospun in DMF/DCM solvent systems allowing to maintain the electrostatic template for long times of production. On the other hand, the fabrication of graded scaffolds with aligned and randomly deposited fibers cannot be obtained from polyelectrolyte solutions due to their high conductivity that prevents the formation of the electrostatic template. In conclusion, whatever the used polymer-solvent system, the on-line measurement of the surface potential allows to track the quality of the electrostatic template which is directly related to the degree of fiber alignment.

3.3. Surface potential in the case of a micropatterned collector

It has been shown that using patterned collectors with protuberances regularly distributed on their surface allows the fabrication of 2D and even 3D structured nanofibrous membranes. This fiber structuration is due to the electrostatic template formed by the suspended fiber strands between the protuberances. Thus, starting from the analysis carried out in the case of a collector having a single gap, the electrospinning of PLA fibers on a regular micro-patterned grid (see Figure 8 and S10) is discussed. Figure 8a shows the evolution of the potential V_{probe} measured by the probe of the electrostatic voltmeter (ESVM) during electrospinning. It is important to note that, as opposed to the previous results obtained for the single gap collector for which V_{probe} was corrected in order to get the average surface potential $\bar{V}_{gap}$ over the suspended fiber strands, here the calibration cannot be performed since a unique $\bar{V}_{gap}$ value has no sense. Thus, due to the fact that the diameter of the probe is much larger than the pitch of the grid, V_{probe} corresponds to an average of the surface potential induced by the suspended fiber strands and the potential of the domains where the fibers are in direct contact with the grid (for which the potential is ~ 0V when the thickness of the deposited fibrous membrane is low). The surface potential was also measured on-line during electrospinning under the same conditions but on a smooth cylindrical collector (*i.e.* without the grid, see Figure 8a, black points). As already discussed, when electrospinning of PLA is carried out on a smooth cylinder, the kinetics of the surface potential follows two stages: (i) a plateau at 0V during a lag time of 10 s and then (ii) a linear increase of the potential being correlated with the amount of charges carried by the deposited nanofiber and the pore size of the fibrous membrane.[32]

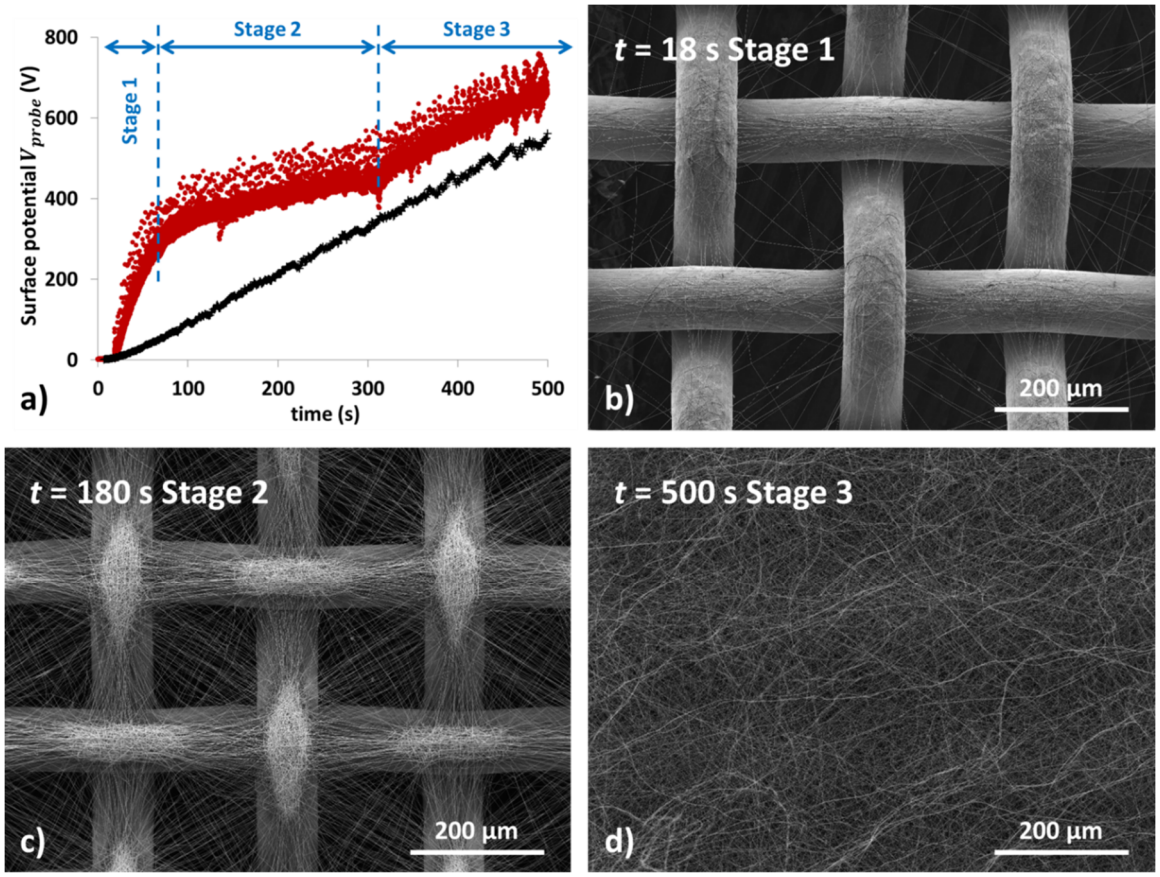

Figure 8. *a) Evolution of the potential V_{probe} measured by the electrostatic voltmeter as a function of time during electrospinning of PLA fibers on a grounded micro-patterned grid (red points) and on a smooth grounded cylinder (black points). SEM pictures of PLA fibers deposited on the grid after b) 18 s, c) 180 s and d) 500 s. Additional SEM pictures obtained at 270 s and 360 s can also be shown in Figure S10 of supporting information.*

When the micro-patterned grid is used instead of the smooth collector, the surface potential follows a completely different trend. In this case, three stages can be observed. The first one, of approximatively 60 s, is subjected to a sharp increase of the surface potential. As opposed to the smooth collector situation for which the potential increases very slowly due to the efficient charge release towards the ground, in the case of the grid, the suspended fiber strands keep their charges with little possibility of dissipation. Figure 8b shows indeed that during this first stage, only few suspended fiber strands are crossing the patterns of the grid, resulting in poor interactions between them. As discussed for the single gap collector during the early period of electrospinning, because there are few interactions between the fiber strands charge dissipation cannot occur. Thus, during the first stage, almost all the charges brought by the deposited suspended strands are accumulated leading to a sharp linear increase of V_{probe}. During the second stage, between 60 s and 300 s, the surface potential increases also linearly but much more slowly than during the previous one. By analogy with the proposed model of charged fibers hanging above a single gap, the attenuation of the slope $\frac{dV_{probe}}{dt}$ can be explained by the interactions occurring between the fiber strands forming closed circuits that reduce the overall electric resistance $R(t)$ of the suspended fibrous layer. Furthermore, the equivalent capacitance C_{coll} of the patterned grid collector is a constant since it depends only on the geometry of the air pockets confined between the metal surfaces of the grid collector and the suspended fibrous layer. Thus, the average relaxation time $\tau(t) = R(t)C_{coll}$ related to the surface potential kinetics during the second stage is lower than in the previous stage. However, as the two kinds of domains (one made of fiber strands suspended above the holes of the grids and the other one

made of fiber strands in direct contact with the grid) are well defined, a perfect electrostatic template is formed. The upcoming fiber being subjected to this electrostatic template, it is preferentially deposited in areas in direct contact with the grid, as these domains are electrically attractive. During this second stage a nice 3D fibrous structuration is obtained (see Figure 8c and S10a in the end of stage 2). However, after longer times of electrospinning (*i.e.* $t \geq 300$ s corresponding to stage 3) the electrostatic template is lost. In this third stage the morphology of the suspended fibrous layer and the one of the fibers in direct contact with the grid lose their structuration and merge into each other (Figure 8d). Indeed, the respective sizes of the closed circuits are of the same order of magnitude (see Figure S10b at the beginning of stage 3). Meanwhile, the deposited thickness increases, resulting in a behavior similar to that observed when electrospinning is performed on a smooth collector. Indeed, as it can be seen, the slope $\frac{dV_{probe}}{dt}$ in the third stage is identical to the one measured during electrospinning on a smooth cylindrical collector. During this last stage, the 3D structuration of the fibers induced by the grid geometry is lost as shown in Figure 8d.

The elaboration of mats with an organized arrangement of the nanofibers find a wide range of applications. Among them, one can cite biomimetic scaffolds for tissue engineering applications,[42] drug delivery devices,[43] smart scaffolds responding under external stimuli,[44] advanced nanofibrous materials for fuel cells and batteries[45] or even hierarchical structure for catalytic applications.[46] The on-line measurement of the surface potential during electrospinning is therefore an efficient tool allowing the control of 2D and even 3D fiber structuration when micropatterned collectors are used for such targeted applications. As the surface potential is linked with the evolution of the fiber organization, its on-line monitoring could help for the controlled fabrication of scaffolds with a gradient of structure throughout their thickness. Such scaffolds with a graded transition between organized fibrous layers and randomly deposited fibers (*e.g.* as observed in Figure 8b-d and S10) or scaffolds having a gradient in pore size[13] are of special interest for the regeneration at interfaces of two tissues (*e.g.* bone to cartilage area).[47] Furthermore, as it was shown that the surface potential depends on the composition of the electrospun solution, it is expected that it could help for the fabrication by multiple-electrospinning (*i.e.* using multiple emitters simultaneously) of composite mats made of different kinds of fibers. In this case, a graded composition of the fibrous structure throughout the thickness of the mat could be obtained with a high level of control. The graded composition could also be characterized based on the position of the ESVM probe to verify the homogeneity of the graded composition across the width of the scaffold. Another topic being of great interest is the elaboration of composites made of nanofibers and microparticles obtained by simultaneous electrospinning and electrospraying. The microparticles can bring to these materials dedicated functionalities such as controlled drug delivery[48] or magnetic or photonic stimuli responsivity for advanced nanomedicine treatments.[44] As in the case of composites made of several types of nanofibers, the on-line measurement of the surface potential could allow the control of the mat's composition throughout its thickness, a key parameter for the fine tuning of the drug release kinetic.[48,49] It has been also demonstrated that the simultaneous electrospraying of microparticles during electrospinning nanofibers allows the fabrication of 3D structured composite when a micropatterned collector made of regularly distributed protuberances is used. The mechanisms leading to the structuration of these composites involves the electrostatic template effect induced by the deposited nanofibers in a similar way as it was explained for electrospinning alone. The main advantage to electrospray microparticles simultaneously with the electrospinning of nanofibers is that (i) the microparticles enhance the electric contact between the fibers and with the protuberances of the collector maintaining thus the electrostatic template effect for longer time of production and (ii) it increases the overall volume of the composite mat.[14] The on-line measurement of the surface potential during such electrospinning/

electrospraying process should allow getting more insight into the mechanism and kinetic of the 3D structuration as a function of the electric properties of the processed material-solvent systems. The control of the architecture of this type of composite is an important prerequisite when biomimetic materials are targeted. As an example, hydroxyapatite microparticles were electrosprayed simultaneously with the electrospinning of PLA giving rise to biomimetic honeycomb-like materials for bone regeneration promoting *in vitro* and *in vivo* osteoconduction, and osteoinduction.[16,17] Hierarchical fibrous carbon catalysts can also be envisaged with such strategy.[46] The periodic deposition of catalytic active phases embedded in the electrosprayed particles allows the growth of carbon nanofibers (CNFs) by subsequent chemical vapor deposition in periodic areas of the carbon composite. While the CNFs increase the overall mechanical properties of the carbon composite, the high porosity of this latter ensures a low pressure drop across its overall thickness during its use as a catalyst.[46]

In conclusion, the on-line measurement of the surface potential is an extremely relevant measurement tool for the characterization of the mat fibrous structure. In combination with other methods such as laser micrometry,[50,51] it could give precious and complementary information on the fibrous structure (*e.g.* pore size, local fiber alignment, variation in thickness, patterned fiber organization…) across all the mat volume which is an important need in a technological point of view.

4. Conclusion

The evolution of the surface potential $\bar{V}_{gap}$ induced by suspended fibers above a single gap during electrospinning was studied in the case of several polymer solutions and gap sizes. A model was proposed in order to get more insight into the involved mechanisms. It was shown that the kinetics of the surface potential is governed by a relaxation time $\tau(t)$ being the product of a time-dependent electric resistance $R(t)$ and a constant capacitance C_{gap}. The latter depends solely on the dielectric properties and geometry of the air pocket trapped below the charged suspended fibrous layer and between the grounded metal walls of the gap collector. The resistance $R(t)$, on the other hand, is correlated with the morphology of the interconnected suspended fiber strands: the denser the suspended fibrous layer (i.e. the smaller the loops made of interconnected fiber strands forming closed RC circuits), the lower the resistance $R(t)$ and consequently the shorter the relaxation time $\tau(t)$. The proposed model was able to estimate the kinetics of the surface potential induced by fiber strands suspended above a single gap which follows three steps. During the first one, the deposited fiber strands do not interact with each other and a strong linear increase of the surface potential is observed. Then, as the density of deposited fibers increases, interactions between the suspended fiber strands induce a decrease of $\tau(t)$ and consequently of $\bar{V}_{gap}$. During the final step, the porous morphology of the suspended fibrous layer reaches a steady state corresponding to a $\bar{V}_{gap}$ plateau. Finally, the evolution of the surface potential was studied when a complex micro-patterned grid collector is used instead of a single gap. It was shown that the kinetics of the surface potential is directly linked with the evolution of the 3D structuration of the nanofibers during electrospinning. At first, well-controlled structures are observed, before structuration is gradually lost and the membrane finally shows a random fiber organization, each structure having its own surface potential signature. In conclusion, the geometry of the collector has a tremendous influence not only on the surface potential but also on its kinetics. Understanding and measuring the surface potential during electrospinning is thus a powerful tool allowing the control of complex 3D structured electrospun mats, finding a broad range of applications.

Acknowledgements

The authors are grateful to the French National Research Agency for the financial support of this work (Project MimHeart project ANR-15-CE08-0010-02). We thank China Scholarship Council (CSC) for the financial support of the PhD student. We also thank Christophe Mélart, Michel Wolf and Thierry Djekriff for their help in the electrospinning set up.

References

[1] D. H. Reneker, A. L. Yarin, *Polymer* **2008**, *49*, 2387.
[2] J. Xue, T. Wu, Y. Dai, Y. Xia, *Chemical Reviews* **2019**, *119*, 5298.
[3] R. T. Weitz, L. Harnau, S. Rauschenbach, M. Burghard, K. Kern, *Nano Lett.* **2008**, *8*, 1187.
[4] K. Sarkar, C. Gomez, S. Zambrano, M. Ramirez, E. de Hoyos, H. Vasquez, K. Lozano, *Materials Today* **2010**, *13*, 12.
[5] J. L. Daristotle, A. M. Behrens, A. D. Sandler, P. Kofinas, *ACS Appl. Mater. Interfaces* **2016**, *8*, 34951.
[6] J. Song, Z. Li, H. Wu, *ACS Appl. Mater. Interfaces* **2020**, *12*, 33447.
[7] D. M. dos Santos, D. S. Correa, E. S. Medeiros, J. E. Oliveira, L. H. C. Mattoso, *ACS Appl. Mater. Interfaces* **2020**, *12*, 45673.
[8] G. C. Dadol, A. Kilic, L. D. Tijing, K. J. A. Lim, L. K. Cabatingan, N. P. B. Tan, E. Stojanovska, Y. Polat, *Materials Today Communications* **2020**, *25*, 101656.
[9] J. Xie, M. R. MacEwan, W. Z. Ray, W. Liu, D. Y. Siewe, Y. Xia, *ACS Nano* **2010**, *4*, 5027.
[10] Z. Ding, A. Salim, B. Ziaie, *Langmuir* **2009**, *25*, 9648.
[11] N. Lavielle, A. Hébraud, C. Mendoza-Palomares, A. Ferrand, N. Benkirane-Jessel, G. Schlatter, *Macromolecular Materials and Engineering* **2012**, *297*, 958.
[12] C.-C. Kuo, C.-T. Wang, W.-C. Chen, *Macromolecular Materials and Engineering* **2008**, *293*, 999.
[13] S. Nedjari, G. Schlatter, A. Hébraud, *Materials Letters* **2015**, *142*, 180.
[14] C. R. Wittmer, A. Hébraud, S. Nedjari, G. Schlatter, *Polymer* **2014**, *55*, 5781.
[15] F. Hejazi, H. Mirzadeh, *Journal of Materials Science: Materials in Medicine* **2016**, *27*, DOI 10.1007/s10856-016-5748-8.
[16] A. Garcia Garcia, A. Hébraud, J.-L. Duval, C. R. Wittmer, L. Gaut, D. Duprez, C. Egles, F. Bedoui, G. Schlatter, C. Legallais, *ACS Biomaterials Science & Engineering* **2018**, *4*, 3317.
[17] M. Naudot, A. Garcia Garcia, N. Jankovsky, A. Barre, L. Zabijak, S. Z. Azdad, L. Collet, F. Bedoui, A. Hébraud, G. Schlatter, B. Devauchelle, J.-P. Marolleau, C. Legallais, S. Le Ricousse, *Journal of Tissue Engineering and Regenerative Medicine* **2020**, *14*, 1570.
[18] Q. Cheng, B. L.-P. Lee, K. Komvopoulos, S. Li, *Biomacromolecules* **2013**, *14*, 1349.
[19] H. Xu, F. Lv, Y. Zhang, Z. Yi, Q. Ke, C. Wu, M. Liu, J. Chang, *Nanoscale* **2015**, *7*, 18446.
[20] H. Mondésert, F. Bossard, D. Favier, *Journal of the Mechanical Behavior of Biomedical Materials* **2021**, *113*, 104124.
[21] N. Pan, J. Qin, P. Feng, B. Song, *Nanoscale* **2019**, *11*, 13521.
[22] J. Xu, C. Liu, P.-C. Hsu, K. Liu, R. Zhang, Y. Liu, Y. Cui, *Nano Letters* **2016**, *16*, 1270.
[23] R. Chen, X. Zhang, P. Wang, K. Xie, J. Jian, Y. Zhang, J. Zhang, Y. Yuan, P. Na, M. Yi, J. Xu, *Nanotechnology* **2019**, *30*, 015703.
[24] S. Nedjari, A. Hébraud, S. Eap, S. Siegwald, C. Mélart, N. Benkirane-Jessel, G. Schlatter, *RSC Adv.* **2015**, *5*, 83600.
[25] A. Zucchelli, D. Fabiani, C. Gualandi, M. L. Focarete, *Journal of Materials Science* **2009**, *44*, 4969.

[26] H. Yan, L. Liu, Z. Zhang, *Applied Physics Letters* **2009**, *95*, 143114.
[27] V. Chaurey, P.-C. Chiang, C. Polanco, Y.-H. Su, C.-F. Chou, N. S. Swami, *Langmuir* **2010**, *26*, 19022.
[28] R. Jalili, M. Morshed, S. A. H. Ravandi, *Journal of Applied Polymer Science* **2006**, *101*, 4350.
[29] D. Li, G. Ouyang, J. T. McCann, Y. Xia, *Nano Letters* **2005**, *5*, 913.
[30] D. Zhang, J. Chang, *Nano Letters* **2008**, *8*, 3283.
[31] D. Mailley, A. Hébraud, G. Schlatter, *Macromolecular Materials and Engineering* **2021**, *306*, 2100115.
[32] M. Liang, A. Hébraud, G. Schlatter, *Polymer* **2020**, *200*, 122576.
[33] M. Santoro, S. R. Shah, J. L. Walker, A. G. Mikos, *Advanced Drug Delivery Reviews* **2016**, *107*, 206.
[34] J. Wróblewska-Krepsztul, T. Rydzkowski, I. Michalska-Pożoga, V. K. Thakur, *Nanomaterials* **2019**, *9*, DOI 10.3390/nano9030404.
[35] K. Belanger, G. Schlatter, A. Hébraud, F. Marin, S. Testelin, S. Dakpé, B. Devauchelle, C. Egles, *Health Science Reports* **2018**, *1*, e86.
[36] H. Ma, C. Burger, B. S. Hsiao, B. Chu, *Journal of Materials Chemistry* **2011**, *21*, 7507.
[37] T. Nakagawa, T. Nakiri, R. Hosoya, Y. Tajitsu, *IEEE Transactions on Industry Applications* **2004**, *40*, 1020.
[38] S. A. Hashmi, A. Kumar, K. K. Maurya, S. Chandra, *Journal of Physics D: Applied Physics* **1990**, *23*, 1307.
[39] R. Mishra, K. J. Rao, *Solid State Ionics* **1998**, *106*, 113.
[40] S. Bongiovanni Abel, F. Montini Ballarin, G. A. Abraham, *Nanotechnology* **2020**, *31*, DOI 10.1088/1361-6528/ab6ab4.
[41] C. Zhu, J. Qiu, S. Thomopoulos, Y. Xia, *Advanced Healthcare Materials* **2021**, *10*, DOI 10.1002/adhm.202002269.
[42] Y. Su, M. S. Toftdal, A. Le Friec, M. Dong, X. Han, M. Chen, *Small Science* **2021**, *1*, 2100003.
[43] M. Zamani, M. P. Prabhakaran, S. Ramakrishna, *Int J Nanomedicine* **2013**, *8*, 2997.
[44] D. Mertz, S. Harlepp, J. Goetz, D. Bégin, G. Schlatter, S. Bégin-Colin, A. Hébraud, *Advanced Therapeutics* **2020**, *3*, 1900143.
[45] C. Xia, Y. Zhou, C. He, A. I. Douka, W. Guo, K. Qi, B. Y. Xia, *Small Science* **2021**, *1*, 2100010.
[46] E. García-Bordejé, Y. Liu, D. S. Su, C. Pham-Huu, *Journal of Materials Chemistry A* **2017**, *5*, 22408.
[47] V. Karageorgiou, D. Kaplan, *Biomaterials* **2005**, *26*, 5474.
[48] M. P. Figueiredo, G. Layrac, A. Hébraud, L. Limousy, J. Brendle, G. Schlatter, V. R. L. Constantino, *European Polymer Journal* **2020**, *131*, 109675.
[49] N. Lavielle, A. Hébraud, L. Thöny-Meyer, R. M. Rossi, G. Schlatter, *Macromolecular Materials and Engineering* **2017**, *302*, 1600458.
[50] Y. Liu, F. Fan, T. Dull, F. J. Chaparro, C. S. Franz, A. Abdalbaqi, C. A. McElroy, J. J. Lannutti, *Polymer* **2020**, *211*, 123044.
[51] Y. Liu, F. J. Chaparro, Z. Gray, J. Gaumer, D. B. Cybyk, L. Ross, J. Gosser, Z. Tian, Y. Jia, T. Dull, A. L. Yarin, J. J. Lannutti, *Polymer* **2021**, *232*, 124120.